2018 Spring Technical Meeting
Central States Section of The Combustion Institute
May 20–22, 2018
Minneapolis, Minnesota

Mode decomposition and convolutional neural network analysis of thermoacoustic instabilities in a Rijke tube

Anthony LoCurto[1,], Tryambak Gangopadhyay[1], Paige Boor[1], Soumik Sarkar[1], and James B. Michael[1]*

[1]Department of Mechanical Engineering, Iowa State University, Ames, IA 50212
[*]Corresponding Author Email: alocurto@iastate.edu

Abstract: Thermoacoustic instabilities are prevalent in a variety of combustion systems including gas turbine combustors and liquid-fueled rocket motors. The limited ability to predict when and how the onset of significant thermo-acoustic instabilities will occur in these systems limits the ability implement active control approaches. The lack of predictive capability and sensing of the onset of instability typically requires the inclusion of passive damping in the combustor design. One possible avenue towards new paradigms in combustor design and optimization is the active control of combustion instabilities. In order to assess the capabilities for detection of combustion instabilities, proper orthogonal decomposition (POD) and a convolutional neural network (CNN) approach are being examined for classification of important dynamics. In this study, high-speed image sequences are collected for a turbulent premixed, bluff-body-stabilized flame in a Rijke tube. The level of thermoacoustic instability is varied through positioning of the flame in the tube. A deep convolutional neural network (CNN) classifies flame images via automatic visual feature. The CNN model is trained on sequential image frames extracted from hi-speed flame videos and demonstrates high accuracy for different flame characteristics from the perspective of instability. The performance of CNN and POD in identifying unstable and stable behavior is evaluated.
Keywords: Thermoacoustic instability, proper orthogonal decomposition, convolutional neural network

1. Introduction

Unstable combustion oscillations have long been of an area of interest, especially for propulsion systems. It has been found that such instabilities can lead to catastrophic failures within a combustion chamber due to the intense pressure fluctuations and excessive heat transfer on the chamber surfaces [1]. Rijke was the first to characterize the coupling between acoustic oscillations and unsteady heat release using a vertical tube open at both ends with a flame or hot gauze in the bottom half of the tube [2]. Rayleigh mathematically modeled this phenomena, and Rayleigh's criterion is used to determine the presence of a combustion instability. If the pressure fluctuation and the unsteady heat release are in phase, then the Rayleigh index will yield a positive value which indicates an instability [1].

Active control systems coupled with an ability to predict the onset of an instability would prove useful in a number of combustion systems in order to mitigate catastrophic failures. Prior work has been done by [3]–[8] of the active control theory and characterization of the onset of thermoacoustic combustion instabilities. Most of these methods have relied on open-loop control

or utilized single-point pressure transducers to provide feedback. Although these techniques are promising, the coupled spatio-temporal dynamics present in turbulent combustion systems may require more advanced capabilities in the detection of the onset of instabilities. Techniques capturing this spatio-temporal behavior offer the potential for improved understanding of this complex dynamical system behavior in order to inform active control strategies [9], [10].

Mode decomposition methods have been used extensively in fluid mechanics and combustion applications to examine relevant dynamics. The use of proper orthogonal decomposition has been applied widely in velocimetry data from both experiments and modeling, and a comprehensive review is given by the monograph of Holmes et al. [11]. POD methods have also been applied in combustion to examine transient multidimensional processes[12]. Schmid et al. have demonstrated the application of dynamic mode decomposition (DMD) in additional fluid mechanics applications [10], [13], where sparsity-promoting DMD has been used to identify the most important dynamical modes [13]. Ghosal et al. analyzed combustion instabilities in a swirl-stabilized dump combustor using sparsity-promoting DMD to identify the most prominent dynamical features of the experimental test data. These techniques have shown promising applications in analysis and dynamical system modeling when applied to both numerical and experimental data [10], [14], [15].

2. Methods / Experimental

Experimental setup

Figure 1 depicts the experimental setup for a Rijke tube configuration coupled with high-speed imaging of the instability region and sound pressure levels in the far-field. An optically-accessible Pyrex tube with an overall length of 2 feet and an outer diameter of 3 inches serves as a Rijke tube. A 3/8-inch stainless steel tube with a conical bluff body attached 0.4 inch above the end of the tube was placed concentric with the Pyrex tube, and served as the burner. The Pyrex tube was attached to a dovetail rail section which allowed adjustment of the Pyrex tube in relation to the fixed burner location. The burner consisted of a premixed composition of ethylene and air with an equivalence ratio of 1.2 and a total flow rate of 19.5 SLPM. The jet exit Reynolds number was approximately 18,000 and the turbulent flame was stabilized using a conical bluff body attached to the tube exit via a sting. The bluff-body stabilized premixed flame resulted in a short flame brush and repeatable behavior of the Rijke tube configuration.

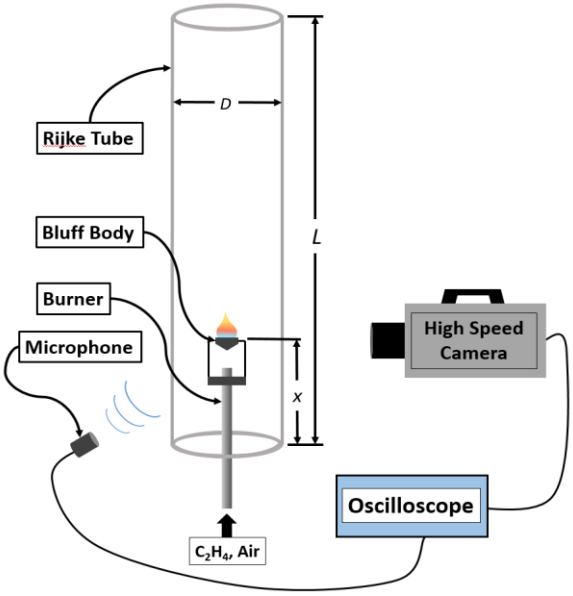

Figure 1: Experimental setup for a Rijke tube configuration with high speed imaging and pressure level acquisition.

The instability was recorded with a high speed camera (Photron FASTCAM SA5) and a microphone (Sony). The high speed camera had a frame rate of 5000 fps with an exposure of 200 μs and a time length of 17 seconds. The microphone was set approximately 12 inches away from the Rijke tube, and connected to and oscilloscope (Tektronix, 4 GHz, 5 MS/s) to measure pressure fluctuations. The oscilloscope also measured the total acquisition time and frame rate of the high speed camera.

In order to ensure steady state conditions within the Rijke tube, data acquisition was delayed by 10 seconds after the flame was ignited. The burner location was changed for each of the five conditions, which can be found in Table 1. Two datasets were acquired for each condition, which produced 34 seconds worth of data. The burner location was changed randomly in order to prevent pattern development between conditions for deep learning training algorithms. The location of burner will be referred to as a non-dimensional value *x/L* because the amplitude of pressure oscillation is correlated to the location of the heat release in relationship to the overall length of the tube.

Table 1: Experimental conditions for burner locations in relationship to the bottom of the Pyrex tube, and the associated non-dimensional location.

Condition Number	Burner Location	x/L
1	3 in.	0.125
2	12 in.	0.500
3	6 in.	0.250
4	0 in.	0.000
5	9 in.	0.375

Proper orthogonal decomposition algorithm

The first step in the POD algorithm is the construction of snapshots by rearranging the images into a series of columns where each image snapshot corresponds to a column of the matrix X and has length corresponding to the number of pixels in the image. The following algorithm is a method of snapshots as commonly used [11], [15]. From the snapshot matrix X, a correlation matrix C can be formed by taking the correlation or covariance between the snapshots making up X. For real-valued data, $X \in R^{m \times n}$ where the number of snapshots is given by the number of columns n and the data from each snapshot is a column of length m. Typically, the length of each snapshot will greatly exceed the number of total snapshots. For example, a sequence of 1000 images where each image is 512×512 pixel^2 will result in dimensions for X of $(m = 512 * 512) \times (n = 1000)$ or 262144×1000.

The covariance matrix is defined as $C = X^*X$, where X^* represents the complex-conjugate of X. Since the elements are real, C can be computed using the transpose: X^TX. In order to determine the POD basis spanning X, the eigenvalue problem for the covariance matrix is solved and the eigenmodes are then projected onto X to form the POD basis. The eigenvalue problem $Cv = C\lambda$ is determined using a singular value decomposition $C = U\Sigma V^*$where the columns of U are the eigenmodes of C and Σ is a diagonal matrix consisting of the corresponding eigenvalues. To find the optimal basis spanning X, the eigenmodes are given by $\psi_k = \phi_k X$, where ϕ_k are the columns of U. This can be represented by the matrix product $\Psi = XU$ to give the full set of eigenmodes forming the POD basis. The eigenvalues are given by the diagonal of Σ.

The energy contained for each mode is often represented by normalizing each eigenvalue λ_k by the sum of all eigenvalues:

$$E_k = \lambda_k / \sum_{j=0}^{n} \lambda_j$$

The cumulative energy fraction including only the first p modes can then be determined by summing over the energy fraction for theses modes

$$E_{cum} = \sum_{k=0}^{\mathrm{p}} E_k$$

representing the amount of 'energy' contained in these modes. This principle is often used to down-select the number of modes required to accurately represent the flow, although typical values for the flame chemiluminescence examined here do not exhibit a clear cutoff. A typical cumulative energy fraction is shown in Figure 2.

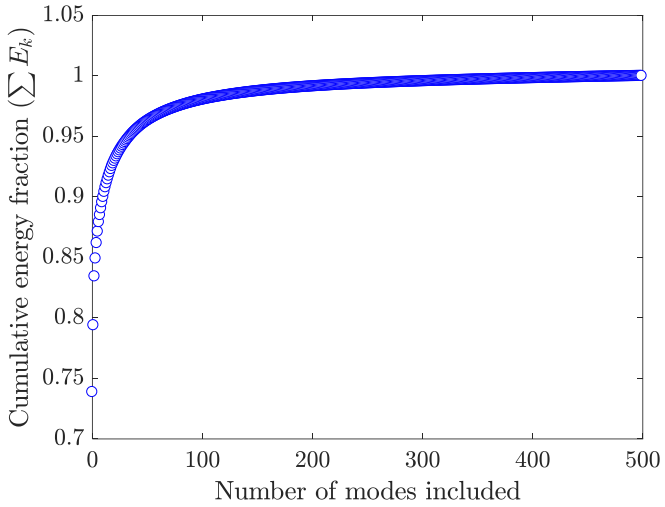

Figure 1: Cumulative energy fraction contained in the first modes included for a POD analysis of 500 consecutive images.

To further examine the POD algorithm, we can look at the spatial modes corresponding to the first few eigenvalues. As explained previously, these are the columns of the matrix product of $\Psi = \Phi X$. The individual eigenmodes are ranked in order of energy content and to display, can be reshaped to the image dimensions to give spatial modes as shown in Figure 2.

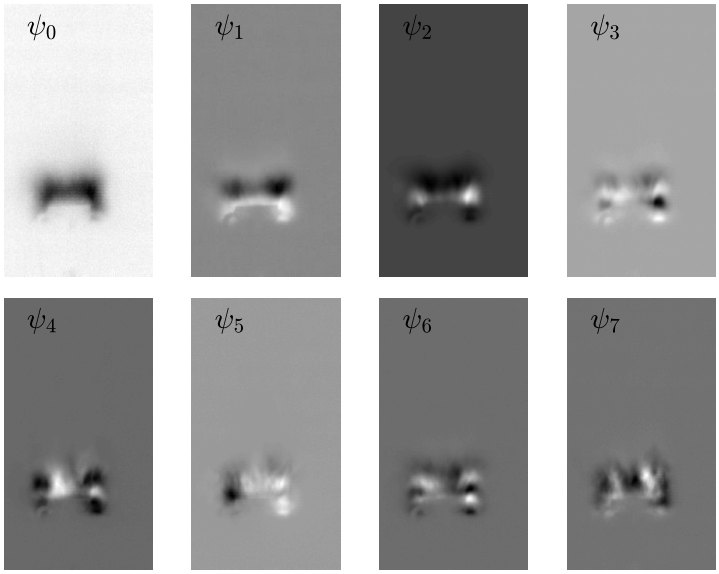

Figure 2: The POD spatial modes 0 through 7.

Using the POD modes, we can also find the content of each spatial mode to each individual time snapshot represented in the collection of snapshots X. The k^{th} snapshot can be fully represented by a linear combination of the eigenmodes as

$$x_k = \sum_{k=0}^{n} a_j \phi_j$$

where coefficients a_j are conveniently available as the rows of the transpose of the second unitary matrix from the SVD, V^*. To get an idea of how much information ('energy') is lost by truncating to a few modes, an instantaneous chemiluminescence image is shown in Figure 3(a) and compared to panels (b) and (c) where a subset of the first 10 and first 20 POD modes are used to approximate the image. As can be seen here, the first 10 modes capture the large scale structure, and the additional modes continue to provide additional structure.

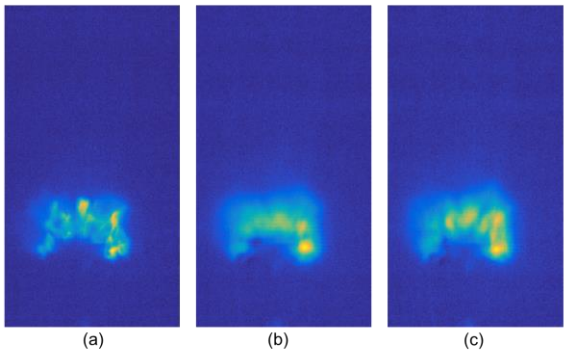

Figure 3: (a) Instantaneous image showing the flame chemiluminescence for a XX ms exposure. (b) The reconstructed single-frame representation using the first 10 POD modes, and (c) the representation using the first 20 POD modes.

For the POD analysis presented in the results section, the thermoacoustic instabilities are examined in the context of the frequency content of the individual POD modes. The time-sequence of content for individual frames for a 0.1 s span is shown in Figure 4(a). Here the coefficients are shown as a function of time as described by $x(t) = \sum_{k=0}^{7} a_j(t)\phi_j$. To examine the actual frequency content of each mode, we present the fast-Fourier transform (FFT) of each mode in Figure 4(b). For this case, the dominant frequency content is evident in mode 0, 1, and 2, with some harmonics prevalent through higher modes. As the mode number continues to increase, the amplitude of these FFT values continues to decrease and in the subsequent analysis only modes 0 to 7 are considered.

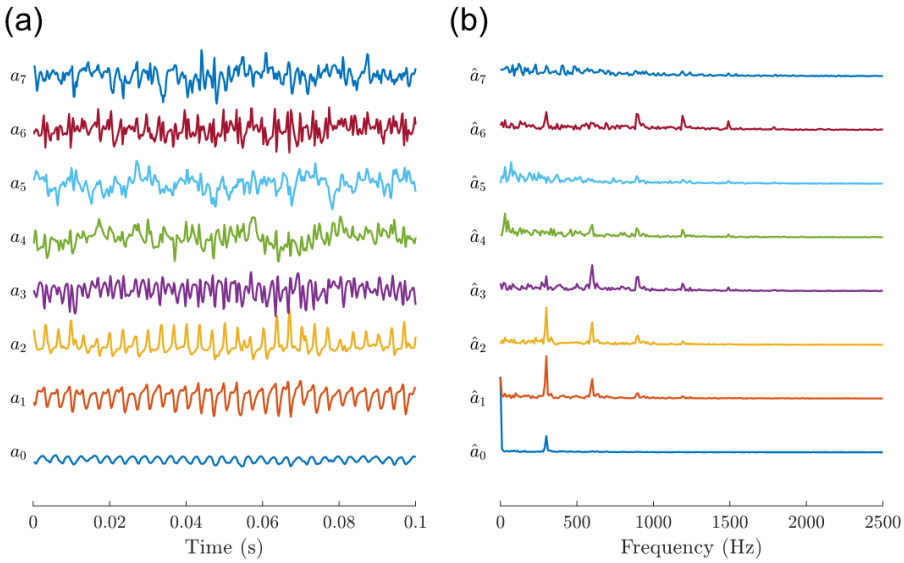

Figure 4: (a) A sample sequence of the mode coefficients ak for a 0.1 second period. (b) The FFT of these mode coefficients showing the predominant narrow-band frequency oscillations are captured by the first few modes.

3. Results and Discussion

In order to characterize the level of thermo-acoustic instability exhibited by the Rijke tube, the acoustic transducer data was analyzed using a windowed FFT. The FFT was run on every 0.1 s interval of the oscilloscope-collected acoustic transducer data. In order to define a metric for the level of sound pressure level, a background-level-normalized instability measure is defined using the integrated FFT between 200-500 Hz and normalized by the background level from 2000-5000 Hz:

$$IM = \frac{\sum_{f=200-500Hz} \hat{P}(f)}{\sum_{f=2000-5000Hz} \hat{P}(f)},$$

where $\hat{P}(f)$ is the FFT of the sound transducer signal $P(t)$. The resulting FFT from a 0.1 s duration window is shown in Figure 5(a) and (b).

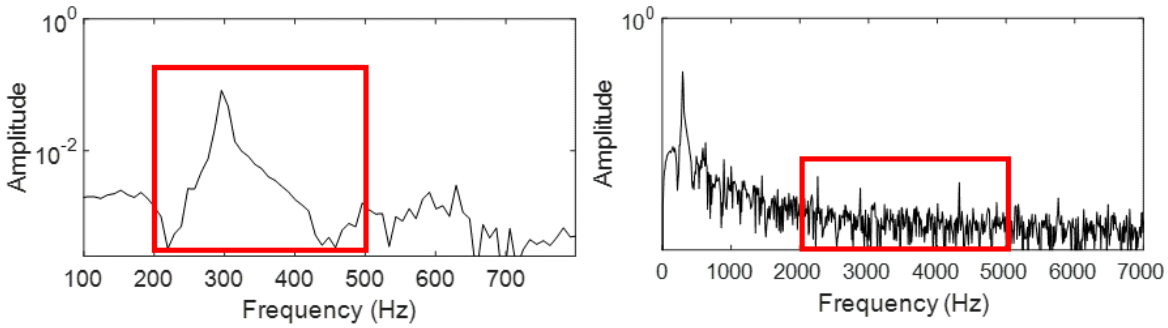

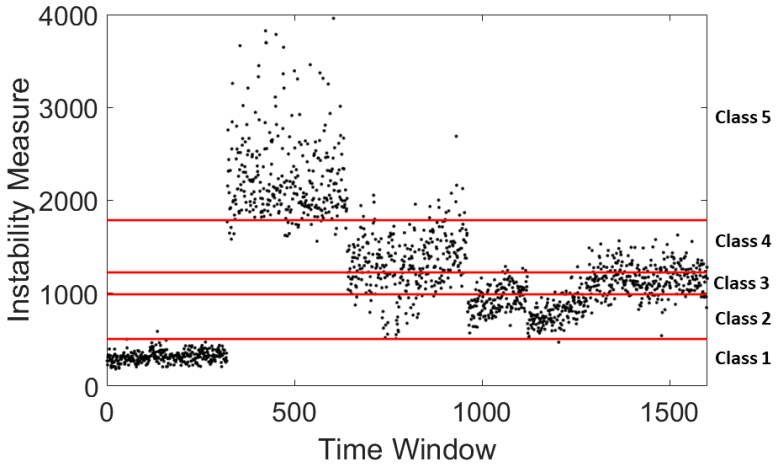

Figure 5: Spectra for the 0.1 s duration windowed FFT are shown with integration regions near (a) the peak thermoacoustic instability frequency and (b) the higher frequency background level. (c) Classification of CNN was made based on this acoustic signal level, dividing into 5 classes shown in.

Details on the algorithm for the convolutional neural network will not be discussed in detail here, but a brief sketch will be given. See [9] and [16] for additional details. A Convolutional Neural Network framework is used to classify images into the 5 classes identified based on the instability measure. The architecture consists of 128 x 128 input images to a supervised model. Two convolutional layers are used, followed by a pooling layer to down-sample features from the previous layers. In this approach [17], max-pooling layers use hyper parameters (non-trained). After the convolutional and pooling layers extract features, fully-connected layers are used to generate non-linear combinations of features and to predict classes. Training of the CNN model is performed with 50,160 training images per class. To examine the accuracy of training, a confusion matrix showing correct and improper classification based on the sound pressure levels (instability measure) is shown in Figure 6. The classification errors for both the strongly unstable and fully stable cases (Class 1 and 5) are excellent, with some degree of confusion (< 20%) between the other classes.

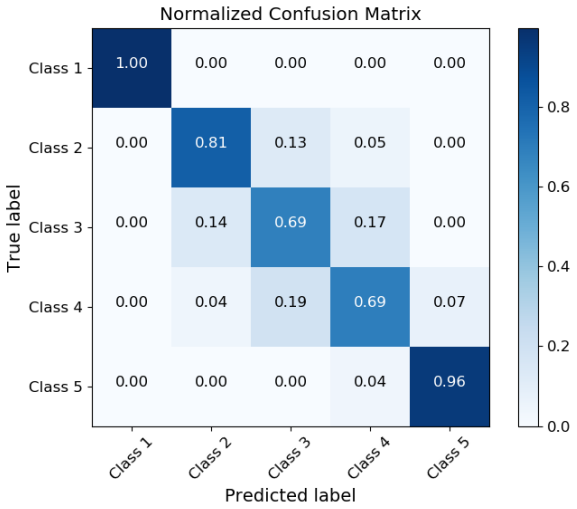

Figure 6: Confusion matrix showing true and predicted classification based noisy classification using sound pressure levels identified from the acoustic measurements.

Figure 7 depicts the relationship between the maximum values for the sum of the first three POD coefficients from the respective FFT and the maximum FFT peak of the sound pressure signal. A window from 150 Hz to 500 Hz was used to capture the first harmonic of the instability frequency. The relative intensity for the POD coefficients and the sound pressure levels were summed over this window. Both cases used 200 ms of data to form their corresponding FFT. A monotonic trend between the two FFT maximums can be found, which is what would be expected because the instability frequency from both the POD analysis and the sound pressure data should increase as the amplitude of the instability grows larger.

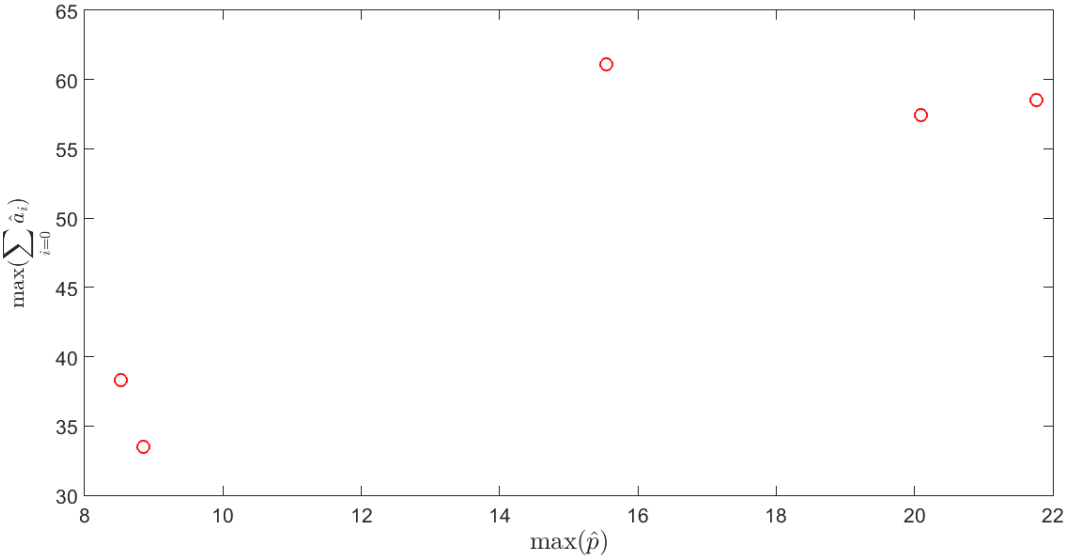

Figure 7: Comparison between maximum POD coefficients values and maximum sound pressure levels from corresponding FFT between 150 Hz and 500 Hz.

High-speed images processed with POD and CNN methods compared to signals obtained from sound pressure levels indicate promising results for forming a basic framework for image-based detection of combustion instability phenomena.

4. Conclusions

The assessment for the use of high-speed image detection for thermo-acoustic instabilities compared to signals obtained from sound pressure levels proves promising for laying the foundation of an active image-based closed loop control system. Results obtained from POD and CNN methods are able to characterize the instability phenomena within a Rijke tube configuration in a similar fashion as the sound pressure levels. Furthermore, the CNN method appears to be able to characterize the instability of an independent dataset based off of a training dataset to a relatively high degree of accuracy. The same methods should be applied to a more realistic combustion chamber since a Rijke tube does not take into account the complex geometry or possibility of multiple instability modes acting within the tube.

5. Acknowledgements

This work has been supported in part by the U.S. Air Force Office of Scientific Research under the YIP grant FA9550-17-1-0220. Any opinions, findings and conclusions or recommendations expressed in this publication are those of the authors and do not necessarily reflect the views of the sponsoring agency.

6. References

[1] K. R. McManus, T. Poinsot, and S. M. Candel, “A review of active control of combustion instabilities,” *Prog. Energy Combust. Sci.*, vol. 19, no. 1, pp. 1–29, 1993.

[2] P. L. Rijke, “Notiz über eine neue Art, die in einer an beiden Enden offenen Röhre enthaltene Luft in Schwingungen zu versetzen,” *Ann. Phys.*, vol. 183, no. 6, pp. 339–343, 1859.

[3] M. A. Heckl, “Active control of the noise from a rijke tube,” *Top. Catal.*, vol. 124, no. 1, pp. 117–133, 1988.

[4] J. Parmentier and T. Poinsot, “Predicting the unstable modes of a simple combustor,” no. index 1, pp. 1–13, 2011.

[5] W. Lang, T. Poinsot, and S. Candel, “Active control of combustion instability,” *Combust. Flame*, vol. 70, no. 3, pp. 281–289, Dec. 1987.

[6] P. J. Dines, “Active control of flame noise,” Clare College, 1984.

[7] J. O’Connor, V. Acharya, and T. Lieuwen, “Transverse combustion instabilities: Acoustic, fluid mechanic, and flame processes,” *Prog. Energy Combust. Sci.*, vol. 49, pp. 1–39, 2015.

[8] G. J. Bloxsidge, A. P. Dowling, N. Hooper, and P. J. Langhorne, “Active Control of Reheat Buzz,” vol. 26, no. 7, 1988.

[9] S. Ghosal, V. Ramanan, S. Sarkar, S. R. Chakravarthy, and S. Sarkar, “Detection and Analysis of Combustion Instability From Hi-Speed Flame Images Using Dynamic Mode Decomposition,” *Vol. 1 Adv. Control Des. Methods, Nonlinear Optim. Control. Robot. Wind Energy Syst. Aerosp. Appl. Assist. Rehabil. Robot. Assist. Robot. Batter. Oil Gas Syst. Bioeng. Appl. Biomed. Neural Syst. Model. Diagnostics Heal. Control Monit. Vibratory Syst. Diagnostics Detect. Energy Harvest. Estim. Identification; Fuel Cells/Energy Storage; Intell. Transp.*, p. V001T12A005, 2016.

[10] P. J. Schmid, “Dynamic mode decomposition of numerical and experimental data,” *J. Fluid Mech.*, vol. 656, pp. 5–28, 2010.

[11] S. Balachandar, *Turbulence, Coherent Structures, Dynamical Systems and Symmetry*, 2nd ed., vol. 36, no. 3. New York: Cambridge University Press, 1998.
[12] S. J. Danby and T. Echekki, "Proper orthogonal decomposition analysis of autoignition simulation data of nonhomogeneous hydrogen-air mixtures," *Combust. Flame*, vol. 144, no. 1–2, pp. 126–138, 2006.
[13] M. R. Jovanović, P. J. Schmid, and J. W. Nichols, "Sparsity-promoting dynamic mode decomposition," *Phys. Fluids*, vol. 26, no. 2, pp. 1–22, 2014.
[14] C. W. Rowley, I. Mezi, S. Bagheri, P. Schlatter, and D. S. Henningson, "Spectral analysis of nonlinear flows," *J. Fluid Mech.*, vol. 641, pp. 115–127, 2009.
[15] J. H. Tu, C. W. Rowley, D. M. Luchtenburg, S. L. Brunton, and J. N. Kutz, "On Dynamic Mode Decomposition: Theory and Applications," no. Dmd, pp. 1–30, 2013.
[16] Y. LeCun and Y. Bengio, "Convolutional networks for images, speech, and time series," *Handb. brain theory neural networks*, vol. 3361, no. April 2016, pp. 255–258, 1995.
[17] S. Sarkar, D. Jha, K. G. Lore, A. Ray, and S. Sarkar, "Multi-modal Spatiotemporal Fusion using Symbolic Causal Modeling for Early Detection of Combustion Instability," pp. 4918–4923, 2016.